Journal of Fluids and Structures 17 (2003) 29–41

JOURNAL OF FLUIDS AND STRUCTURES

www.elsevier.nl/locate/jnlabr/yjfls

Numerical investigation of transonic limit cycle oscillations of a two-dimensional supercritical wing ☆

L. Tang[a,*], R.E. Bartels[b], P.-C. Chen[a], D.D. Liu[c]

[a] *ZONA Technology, Inc., Scottsdale, AZ 85251-3540, USA*
[b] *NASA Langley Research Center, Hampton, VA 23681-0001, USA*
[c] *Arizona State University, Tempe, AZ 85287-6106, USA*

Received 17 May 2001; accepted 8 July 2002

Abstract

CFD-based aeroelastic computations are performed to investigate the effect of nonlinear aerodynamics on transonic limit cycle oscillation (LCO) characteristics of the NLR7301 airfoil section. It is found that the LCO solutions from Navier–Stokes computations deviate less from the experiment than an Euler solution but strongly depend on the employed turbulence model. The Degani–Schiff modification to the Baldwin–Lomax turbulence model provokes spurious vorticity spots causing multiple shocks which might be unphysical, while the Spalart–Allmaras turbulence model yields physically reasonable unsteady shocks. In the cases examined, smaller initial perturbations lead to larger LCO amplitudes and vice versa, in contradiction to what one might expect. The amplitude of the initial perturbation is also found to have an impact on the mean position of LCO. Also addressed in the paper are aspects of multiblock message passing interface (MPI) parallel computation techniques as related to the present problem.
Published by Elsevier Science Ltd.

1. Introduction

Limit cycle oscillation (LCO) has been a prevalent aeroelastic problem on several current fighter aircraft configurations. The phenomenon usually occurs for aircraft with external stores throughout, but not limited to, the transonic flight regime (Denegri, 2000; Norton, 1990; Chen et al., 1998; Cunningham and Meijer, 1995), although a business jet wing LCO was also reported recently (Edwards, 1996; Edwards et al., 2001). Complicated by the problem geometry, e.g., the aircraft-store system, the LCO mechanisms still remain to be fully understood. In fact, there exist few analytical techniques available for LCO prediction and an insufficient understanding of its physics.

With aerodynamic feedback, LCO is sustained periodic oscillation which neither increases nor decreases in amplitude over time for a given flight condition. A series of researchers, notably Cunningham and Meijer (1995), believe that the wing/store LCO is a purely aerodynamic phenomenon, largely due to transonic shock oscillation and shock induced flow separation. This LCO scenario, which is sometimes referred to as the transonic shock/separation (TSS) model, has been suggested by Edwards to be, with viscous effects, one of the major factors contributing to transonic LCO for wings (Edwards, 1996; Edwards et al., 1983). On the other hand, Chen et al. (1998) proposed a radically different LCO model based on the observation that wing/store LCO can be a post-flutter phenomenon whenever the flutter mode contains low unstable damping. This type of flutter mode is called a "*hump mode*". Since the aircraft structure usually exhibits some structural nonlinearities, such as friction, free-play, etc., the moderate growth of amplitudes corresponding to the

☆ Presented at the 42nd AIAA/ASME/ASCE/AHS/ASC Structures, Structural Dynamics, and Materials Conference, Seattle, WA, April 16–19, 2001.

*Corresponding author. Tel.: +1-480-945-9988; fax: +1-480-945-6588.
E-mail address: tangl@zonatech.com (L. Tang).

0889-9746/03/$ - see front matter Published by Elsevier Science Ltd.
PII: S0889-9746(02)00114-7

low negative aerodynamic damping may be suppressed. The result is then a steady state oscillation. This is sometimes referred to as the nonlinear structural damping (NSD) model of the aeroelastic LCO. Although not proven through experimental tests or numerical simulations, results of the NSD model show excellent correlation with flight test LCO data of a F-16 fighter configuration throughout subsonic and transonic Mach numbers (Chen et al., 1998; Mignolet et al., 1999). It should be noted that the TSS and NSD models could either be sole agent of or could both contribute to the observed LCO.

Recent renewed interest in LCO is perhaps motivated by the need to further understand the physics of LCO along with the current implementation of CFD methodology in aeroelasticity. Among the potential computational methods for LCO prediction/investigation, two will be mentioned here: the CFL3D code (version 6) (Biedron, 2002; Krist et al., 1997; Bartels, 2000) developed and supported by NASA/Langley, and the proper orthogonal decomposition-based reduced order model approach (Hall et al., 1999) originated by Dowell and Hall of Duke University. The former is a conventional time-domain CFD method whereas the latter a frequency-domain CFD-based technique.

The present study uses a CFD time-marching method, CFL3D v6, to numerically investigate the transonic aeroelastic LCO behavior of a supercritical airfoil section in conjunction with a two-degree-of-freedom plunge/pitch structural model (Schewe and Deyhle, 1996; Knipfer et al., 1998; Knipfer and Schewe, 1999). It is reasonable to start with investigating a two-dimensional LCO case in order to better understand the physics of LCO. However, because of the complexity of a two-dimensional LCO experimental test, there is very little experimental data available for comparison. To the best of our knowledge, the work performed by Schewe's group in DLR (Schewe and Deyhle, 1996; Knipfer et al., 1998; Knipfer and Schewe, 1999) is perhaps the only two-dimensional LCO experimental data currently available in the literature. Those test data have in fact been used by Platzer's group (Weber et al., 2001; Castro et al., 2000) to validate their thin-layer Navier–Stokes aeroelastic solver. While the emphasis of Weber et al. (2001) and Castro et al. (2000) was on the predictive capability of the thin-layer Navier–Stokes aeroelastic solver, our emphasis here is to investigate the impact of nonlinear aerodynamics, such as the viscosity, turbulence modelling and the initial perturbation size, on the computed transonic LCO behavior of the supercritical airfoil, the topics of the TSS model. On the other hand, the employed structural model is still linear. Also addressed in the paper are the issues related to multiblock MPI parallelization aspects of the aeroelastic computations.

2. Numerical methodology

CFL3D v6 solves the thin-layer Reynolds averaged Navier–Stokes equations. In the present computations, the inviscid terms are computed using the flux-difference splitting method of Roe (1981) and a third-order upwind-biased spatial differencing with flux limiting in the presence of shocks. The viscous terms are discretized using second-order central differencing. For time discretization, first-order backward differencing is used for steady calculations while second-order backward differencing with pseudo-time subiterations is used for static and dynamic aeroelastic calculations. The employed turbulence models are the Spalart–Allmaras model (Spalart and Allmaras, 1992) and the Baldwin–Lomax model with the Degani–Schiff modification (Degani and Schiff, 1983). A detailed description of the code can be found in Krist et al. (1997).

One of the most important features of the CFL3D v6 code is its capability to simultaneously compute solutions on multiple zone grids with one-to-one connectivity by using the parallel MPI routines. Spatial accuracy is maintained at zone boundaries, although subiterative updating of boundary information is required. Coarse-grained parallelization using the MPI protocol can be utilized in multiblock computations by solving one or more blocks per processor. As a result, the time required for a CFD-based aeroelastic computation can be drastically reduced. When there are more blocks than processors, optimal performance is achieved by allocating an equal number of grid points to each processor.

In this paper, both single and multiblock MPI parallel aeroelastic computations near the onset of flutter LCO are compared with experiment and with other computations. Fig. 1 shows the C-type grid with 273×93 mesh points around the NLR7301 airfoil that has been divided into eight 69×47 blocks. This and a single block version of the grid are used in the computations to follow.

In order to accommodate multiblock computations, the mesh deformation scheme employed in Bartels (2000) is slightly modified. In Bartels (2000), the remeshing scheme uses a modified spring analogy with solid body translation/rotation of the fluid mesh near solid surfaces. Initialization of the grid deformation at each time step is performed using a transfinite interpolation (TFI) step. The mesh interior is then smoothed using the modified spring analogy.

In the present implementation, the subgrid-based TFI scheme of Hartwich and Agrawal (1997) has been employed for grid initialization at each time step. This method uses subgrids consisting of "slave vertices" to move both block

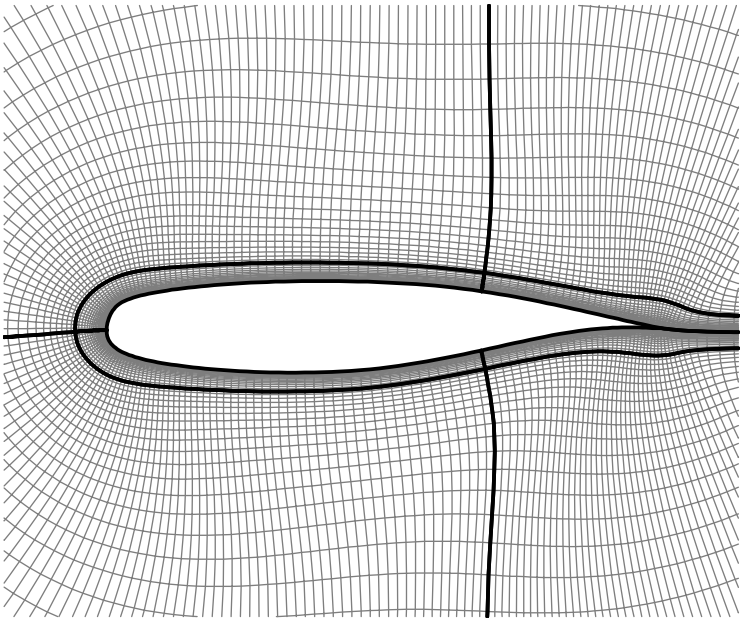

Fig. 1. Multiblock C-type grid around NLR 7301 airfoil (eight 69×47 blocks).

boundaries and interiors. In some instances, in order to achieve an optimal division of grid points, it is necessary to place flow field block boundaries near a moving solid surface. An example of this is shown in Fig. 1. The multiblock boundary and interior movement scheme allows the user to place block boundaries near surfaces as necessary for optimal parallelization. Boundaries interior to the fluid domain near a surface respond to the local surface motion. As the airfoil moves, block boundaries move to maintain integrity of block interfaces and the airfoil surface.

Users have the option to specify whether to update the grid using this subgrid/TFI-based scheme alone, or to update the grid with an initialization using this scheme plus additional smoothing steps. These added smoothing steps, the number of which can be defined by the user also, employ the modified spring analogy scheme (Bartels, 2000). In the current implementation, the spring analogy scheme updating the mesh interior is now written in delta formulation so that the relative orientation of the original grid is retained. The solid body rotation/translation of the fluid grid is also now performed near both solid surface and block fluid boundaries.

The time-marching simulation of the aeroelastic system is conducted using the state transition matrix solution from t to $t + \Delta t$ of the state variable representation of the decoupled modal equations (Edwards et al., 1983; Cunningham et al., 1988). The state transition matrix-based scheme is optimal in the sense that it is derived from an exact solution of the free response of the modal equations. The actual scheme uses a predictor/corrector procedure. The predictor step marches the structure using the solution of the modal equations at the time step n to get the surface deflection at the time step $n + 1$. This provides the surface shape for a recomputation of the fluid mesh and the fluid domain solution at $n + 1$. After a solution of the fluid domain involving multiple subiterations, the corrector step then solves the modal equations at the time step $n + 1$ using the averaged generalized forces at n and $n + 1$.

Because the CFD and CSM meshes usually do not match at the interface, CFD/CSM coupling requires a surface spline interpolation between the two domains. The conservative interpolation of CSM mode shapes to CFD surface grid points is done as a preprocessing step. Modal deflections at all CFD surface grids are first generated. Modal data at these points are then segmented based on the splitting of the flow field blocks. Mode shape displacements located at CFD surface grid points of each segment are used in the integration of the generalized modal forces and in the computation of the deflected surface. The final surface deformation at each time step is a linear superposition of all the modal deflections.

The following is an account of our theoretical modelling of Schewe's experiment on transonic flutter of a two-dimensional supercritical wing with an NLR7301 airfoil section (Schewe and Deyhle, 1996; Knipfer et al., 1998; Knipfer and Schewe, 1999). Fig. 2 depicts a simplified model of the two-degree-of-freedom test set-up. The two-dimensional wing has a chord length of 0.3 m ($c = 0.3$ m) and a span of 1 m ($b = 1$ m). The plunge spring and the pitch spring are

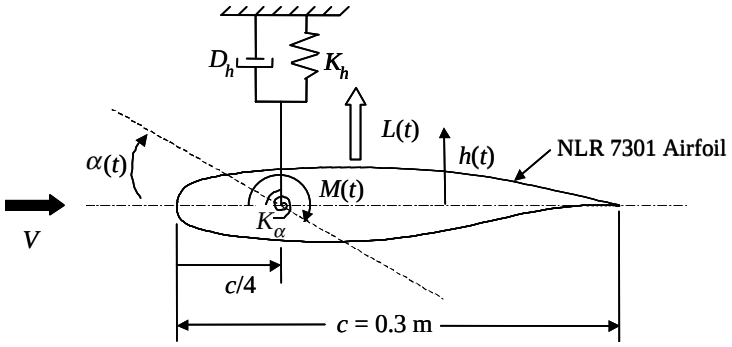

Fig. 2. Two-degree-of-freedom dynamic model.

attached to the same $c/4$ position. The corresponding two-degree-of-freedom equation of motion of the set-up reads as

$$\begin{bmatrix} m_h & -s_\alpha \\ -s_\alpha & I_{c/4} \end{bmatrix} \begin{Bmatrix} \ddot{h} \\ \ddot{\alpha} \end{Bmatrix} + \begin{bmatrix} D_h & 0 \\ 0 & D_\alpha \end{bmatrix} \begin{Bmatrix} \dot{h} \\ \dot{\alpha} \end{Bmatrix} + \begin{bmatrix} K_h & 0 \\ 0 & K_\alpha \end{bmatrix} \begin{Bmatrix} h \\ \alpha - \alpha_0 \end{Bmatrix} = \begin{Bmatrix} L(t) \\ M(t) \end{Bmatrix}, \tag{1}$$

where m_h is the total mass ($m_h = 26.64\,\text{kg}$), $I_{c/4}$ is the mass moment of inertia about $c/4$ ($I_{c/4} = 0.086\,\text{kg m}^2$), s_α is the static unbalance ($s_\alpha = 0.378\,\text{kg m}$), D_h and D_α are the damping factors of the plunge motion (h) and the pitch motion (α), respectively ($D_h = 82.9\,\text{kg/s}$ and $D_\alpha = 0.197\,\text{kg m}^2/\text{rad/s}$), K_h and K_α are the stiffness of the plunge spring and the pitch spring, respectively ($K_h = 1.21 \times 10^6\,\text{N/m}$ and $K_\alpha = 6.68 \times 10^3\,\text{N m/rad}$), and $L(t)$ and $M(t)$ are the aerodynamic lift and moment, respectively, in Newton and Newton-meter.

The aeroelastic equations and the CFD grid are maintained in dimensional form. To perform the time-marching CFD computation in CFL3D v6, it is necessary to convert Eq. (1) into modal coordinates, i.e.,

$$\begin{Bmatrix} h \\ \alpha \end{Bmatrix} = [\phi]\{q\}, \tag{2}$$

where q is the modal coordinate and ϕ is the modal matrix of the undamped structure. For this numerical example we have

$$\phi = \begin{bmatrix} -0.1735 & 0.1004 \\ 0.9277 & 3.403 \end{bmatrix}. \tag{3}$$

Substituting Eq. (2) into Eq. (1) and pre-multiplying the resulting equation by ϕ^{T} yields

$$[I]\{\ddot{q}\} + \begin{bmatrix} 2\omega_h\zeta_h & 0 \\ 0 & 2\omega_\alpha\zeta_\alpha \end{bmatrix} \{\dot{q}\} + \begin{bmatrix} \omega_h^2 & 0 \\ 0 & \omega_\alpha^2 \end{bmatrix} \{q\} = \phi^{\mathrm{T}} \begin{Bmatrix} L(t) \\ M(t) \end{Bmatrix}, \tag{4}$$

where ω_h and ω_α are the undamped natural frequencies of the plunge and pitch motions, respectively ($\omega_h = 205.4\,\text{rad/s}$ and $\omega_\alpha = 299.3\,\text{rad/s}$), ζ_h and ζ_α are the plunge and pitch damping ratios, respectively ($\zeta_h = 0.00649$ and $\zeta_\alpha = 0.00521$). Note that the off-diagonal terms in the damping matrix are assumed to be zero for simplicity.

3. Results and discussion

The case simulated is measurement no. 77 documented in Knipfer et al. (1998). As mentioned before, the experimental model is a two-dimensional supercritical wing with the NLR7301 airfoil section. The chord length of the wing is 0.3 m and the mean angle of attack is 1.28°. The experimental conditions are the free-stream Mach number of 0.768 and the Reynolds number of 1.727×10^6 based on the chord length. A transonic LCO in two degree of freedom is experimentally observed at a dynamic pressure of 0.126 bar. The corresponding free-stream velocity is 254.7 m/s, and the total pressure is 0.45 bar.

3.1. Time-averaged surface pressure distribution

As pointed out in Weber et al. (2001) and Castro et al. (2000), due to the relatively large chord length of the airfoil with respect to the wind tunnel test-section (1 m × 1 m), both the free-stream Mach number and the angle of attack need to be corrected in the computations in order to take into account wind tunnel wall effects if the tunnel wall boundary conditions are not explicitly introduced. The criterion used in Weber et al. (2001) and Castro et al. (2000) is to make corrections in such a manner that the computed and measured time-averaged surface pressure distribution match. In this way, a wind tunnel wall correction is realized in a certain averaged sense.

Computations are performed to search the flow conditions which best meet the wind tunnel conditions in the computations with the different flow models. An Euler computation is first performed on a C-type grid with 273×61 points. The best agreement with the experimental data is found at $M_\infty = 0.734$ and $\alpha = -0.25^\circ$. Fig. 3 indicates that even for this corrected Mach number and the corrected angle of attack, the predicted shock strength is stronger than the experimental result, and the location of the shock is behind the measured one. It appears to be impossible to match both the measured strength and location of the shock using the Euler computation. Two viscous computations are then performed on a C-type grid with 273×93 points. One uses the Degani–Schiff modified Baldwin–Lomax turbulence model (B–L–D–S), and the other uses the Spalart–Allmaras turbulence model (S–A). The corrected Mach number is found to be 0.748 for both models while the corrected angle of attack is -0.02° for the B–L–D–S model and 0.15° for the S–A model. It can be seen in Fig. 3 that both viscous results have much closer agreement with the experimental data, especially for the shock strength and location, clearly showing that viscous effects are crucial for accurate modelling.

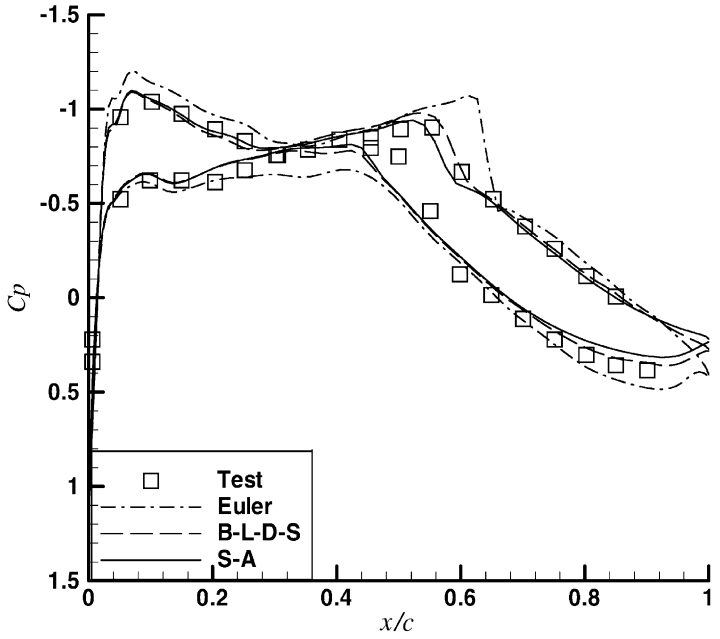

Fig. 3. Time-averaged surface pressure distribution (spring-off).

Table 1
Initial conditions for LCO computations

Method		M_∞	α (deg)
Euler	Spring-off	0.734	−0.25
	Spring-on	0.734	−0.1
B–L–D–S	Spring-off	0.748	−0.02
	Spring-on	0.748	0.15
S–A	Spring-off	0.748	0.15
	Spring-on	0.748	0.32

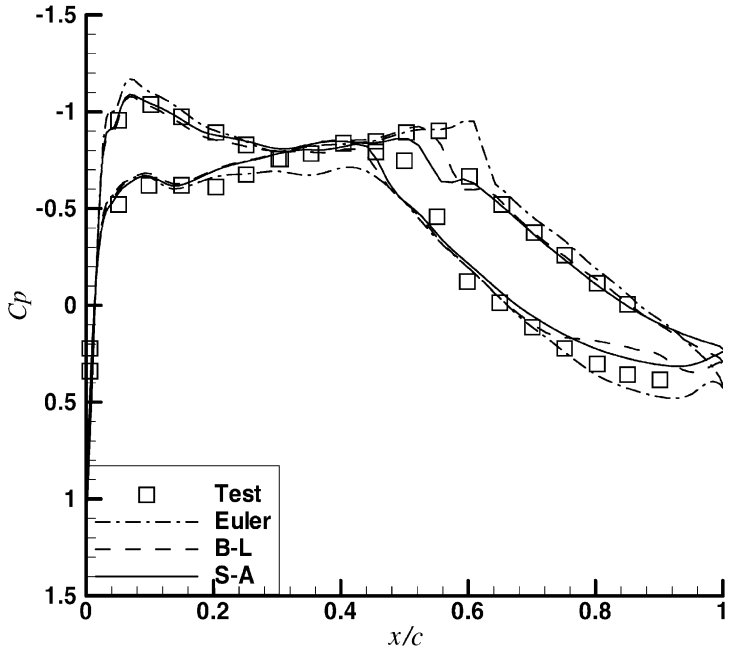

Fig. 4. Time-averaged surface pressure distribution (spring-on).

(a) By B-L-D-S model (b) By S-A model

Fig. 5. Entropy contours (spring-on): (a) by B–L–D–S model; (b) by S–A model.

The above computed results are for the spring-off condition, in which the wing is assumed as rigidly mounted in the computation. By taking into account the contribution from the structural flexibility (the spring-on condition), the corrected angle of attack becomes -0.1° for the Euler computation, 0.15° for the B–L–D–S viscous model, and 0.32° for the S–A viscous model, while the corrected Mach number does not change. This is because, for a two-dimensional model, structural flexibility only affects the rotation of the model. These corrected Mach numbers and angles of attack for the spring-on conditions (see Table 1) will be used as inputs for further dynamic aeroelastic computations except those in the next section, where the conditions of Weber et al. (2001), the corrected Mach number of 0.753 and the corrected angle of attack of 0.6°, are used in order to compare our computed flutter results with theirs under the same conditions.

One important phenomenon in Fig. 4 is that the B–L–D–S model produces a pressure or lift loss on the lower surface near the trailing edge, which is not found in Fig. 3, the spring-off condition. In order to understand the mechanism behind this phenomenon, Fig. 5 presents the entropy contours given by the two turbulence models. It is found that the B–L–D–S model seems to produce spurious vorticity on the lower surface near the trailing edge.

3.2. Performance and time-step convergence

The static aeroelastic case is used to compare run times between the single block/sequential, eight block/sequential, and eight block/MPI parallel computations. Starting from a steady state a time-accurate aeroelastic solution is marched for 800 time steps with five multigrid subiterations each. The S–A turbulence model is used in each case.

Table 2
Cost/performance

Grid/computational type	TFI	Spring analogy smoothing	CPU time/processor (s)
1 block/sequential	Yes	Yes	8800
8 block/sequential	Yes	Yes	5430
8 block/MPI	Yes	Yes	690
8 block/MPI	Yes	No	680
8 block/MPI[a]	No	No	610

[a] Also without aeroelasticity.

Table 3
Flutter results

	a_h (mm)	a_α (deg)	f (Hz)
$\Delta t = 0.128$	11.2	3.72	34.5
$\Delta t = 0.040$	9.17	3.24	34.3
$\Delta t = 0.0125$	8.99	3.17	34.3
Weber et al. (2001)	10.5	4.09	33.42
Experiment	0.65	0.18	32.85

Table 2 gives computational performance results for various grids, run modes, and code configurations. The first two rows correspond to sequential computations of the single and eight block versions of the grid. The eight-block grid takes 28% less CPU time than the single-block grid on a SGI Origin 2000 machine, apparently due to better caching of the smaller sized blocks. The parallel computation with eight processors runs 7.8 times faster than the same run sequentially, clearly showing the time saving by parallel computation. The last two rows present the computational effort required for the spring analogy-based smoothing step, and the TFI grid movement along with the aeroelastic computation. Three iterations of the spring analogy scheme add about 1.5% computing time to the solution, and the TFI grid movement along with the aeroelastic computation adds about 10% to the run time.

Table 3 shows the computed flutter amplitudes and frequency based on the single-block grid using successively smaller time-step sizes. These results are further compared with the computed flutter results of Weber et al. (2001) and the experimental data of Knipfer et al. (1998). Following the computations of Weber et al. (2001), the LCO computations here are also performed at $M = 0.753$, $\alpha = 0.6^\circ$, and a dynamic pressure of 0.126 bar, using the S–A model. Initialization is accomplished with a static aeroelastic solution followed by an initial perturbation of -0.00114 in the velocity of the second structural mode for the dynamic simulation. The chosen time-step sizes result in 80, 250, and 800 time steps per plunge/pitch cycle. Nine subiterations per time step are used. Columns two and three are half amplitudes of the fully developed LCO plunge and pitch motions, while column four is the plunge/pitch frequency. As can be seen in Table 3, our computed flutter results are comparable with those of Weber et al. (2001). While our computed flutter amplitudes at smaller time-step sizes are slightly more accurate, the computed flutter frequencies of Weber et al. (2001) are slightly closer to the experiment. It is expected that with smaller time-step sizes, the computed flutter amplitudes and frequency are closer to the experimental data. However, even with the smallest time-step size, the computed flutter amplitudes are still one order of magnitude larger than the experimental data. This is possibly because the wind tunnel wall boundary conditions are not explicitly introduced into the computation. Readers are referred to Castro et al. (2000) for the computed LCO results from the computations with the explicit implementation of tunnel wall boundary conditions. Another possible reason is that although the structural characteristics of the test model is two dimensional, the three-dimensional aerodynamic effect, which is missing in our two-dimensional CFD simulation, is important because of the relatively large chord length of the airfoil with respect to the wind tunnel test-section.

The above flutter amplitudes and frequencies are computed based on a sampling of the last 8–10 cycles of motion in which the data appears to eventually converge to an LCO for the two smaller time-step sizes. For the largest time-step size, however, the computed amplitudes continue to slowly grow even after 100 cycles. Therefore, the smallest time-step size with nine multigrid subiterations is used for all of the remaining dynamic computations presented.

The speed increase offered by computing in parallel is appealing. There is however trade-offs when using coarse grain parallelization. As can be seen from Fig. 6, the amplitude and frequency of the multiblock plunge and pitch motions eventually converge to the values virtually identical to that of the single block grid ($a_h = 8.87$ mm, $a_\alpha = 3.13^\circ$, $f = 34.3$ Hz). However, the time at which the LCO can be considered as converged is different between the two

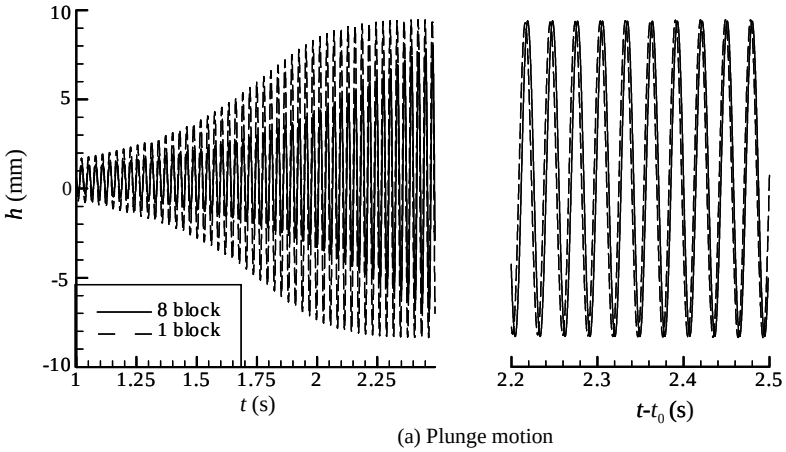

(a) Plunge motion

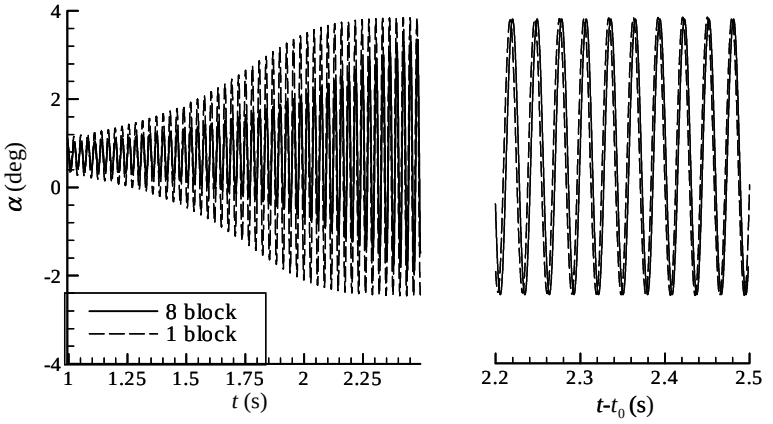

(b) Pitch motion

Fig. 6. Comparison of single/multiblock grid computation (N–S, $M_\alpha = 0.753$, $\alpha = 0.6^\circ$), $t_0 = 0$ s (1 block), $t_0 = 4.5$ s (8 blocks): (a) plunge motion; (b) pitch motion.

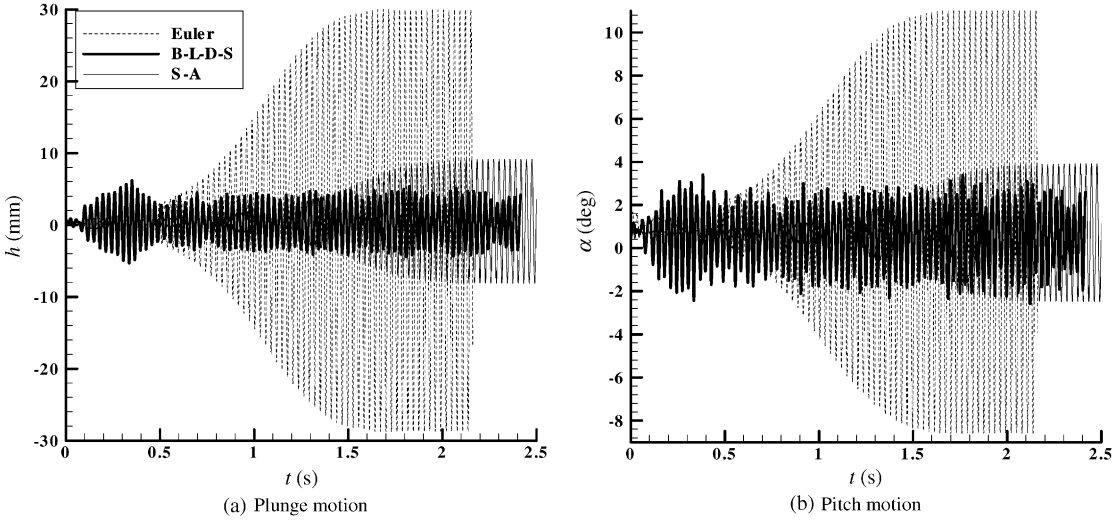

(a) Plunge motion (b) Pitch motion

Fig. 7. LCO predicted by Euler/N–S methods: (a) plunge motion; (b) pitch motion.

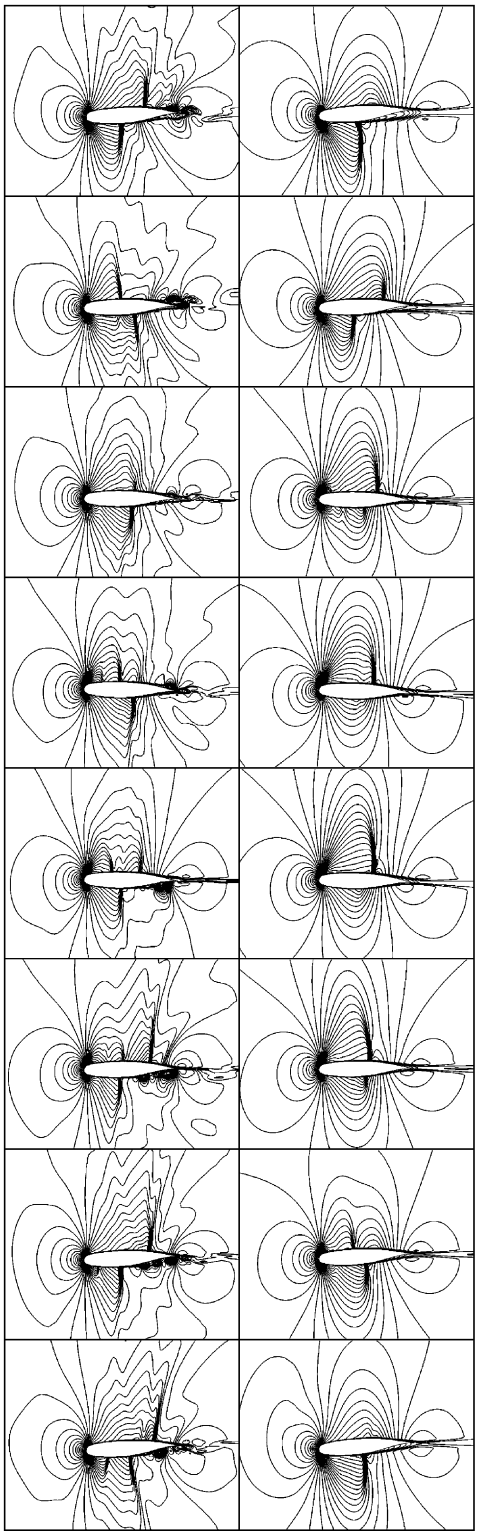

(a) By B-L-D-S model (b) By S-A model

Fig. 8. Predicted density contours: (a) by B–L–D–S model; (b) by S–A model.

computations, and this accounts for the different values of t_0 for the single block and eight block computations. It can be seen that the LCO computed with eight flow field blocks takes much longer to develop than does an identical LCO computed on a single flow field block. So, all of the following dynamic computations are based on a single block grid.

3.3. Effect of viscosity and turbulence modelling

Fig. 7 compares LCO predicted by Euler and Navier–Stokes methods. It is found that although both inviscid and viscous computations are able to predict LCO, the amplitude of LCO predicted by the viscous computations is less than $\frac{1}{3}$ of that predicted by the inviscid computation, much closer to the experimental data. This indicates that as one would expect, it is important to include the viscous terms in LCO computations to limit the amplitude of the flutter LCO.

Also shown in Fig. 7 is the difference between the computed LCO by the two viscous methods. It is found that the B–L–D–S model reaches large amplitude limit cycle quite rapidly. Plunge and pitch amplitudes of the B–L–D–S result are approximately 4 mm and 2°, respectively, and the predicted frequency is 32.2 Hz. On the other hand, the S–A model reaches LCO much later. Its plunge and pitch amplitudes are larger than those given by the B–L–D–S model, around 9 mm and 3°, respectively. Furthermore, the B–L–D–S LCO is random/chaotic while the S–A LCO is periodic. It can be seen that the specific turbulence model used can significantly alter the nature of the LCO solution.

In order to understand the mechanism behind the differences caused by the two turbulence models, Fig. 8 further presents the predicted density contours at 8 time steps uniformly distributed in the last cycle. The B–L–D–S results presented at the left-hand side clearly show multishocks with large excursions possibly caused by spurious vorticity spots. This is why the B–L–D–S LCO exhibits chaotic behavior. On the other hand, no visible vorticity spots are found in the S–A results presented at the right-hand side. As a result, the flow pattern is much more regular. It is noteworthy that smaller time-step sizes and more subiterations have been tested for the B–L–D–S model but the difference of the results are not visible. It is possible that the current implementation of the Degani–Schiff modification to the Baldwin–Lomax model in CFL3D v6 code somehow causes spurious vorticity spots.

3.4. Effect of perturbation size

The above LCO computations are performed with a small initial perturbation, −0.0012 in the velocity of the first mode, which is about 0.0082% of the free-stream speed. In order to investigate the effect of initial perturbation size on the resulting LCO, the earlier S–A viscous computations are repeated with the two larger initial perturbations. The one referred to as the medium perturbation in Figs. 9 and 10 has five times of the original perturbation size, and that referred to as the large perturbation has 10 times of the original perturbation size.

Fig. 9 indicates that compared to the small perturbation, LCO occurs earlier, and the amplitudes of both plunge and pitch modes are slightly reduced for the medium perturbation. Further increasing the perturbation size by two, a damped solution is achieved. This is contradictory to what one might expect. In order to understand the above

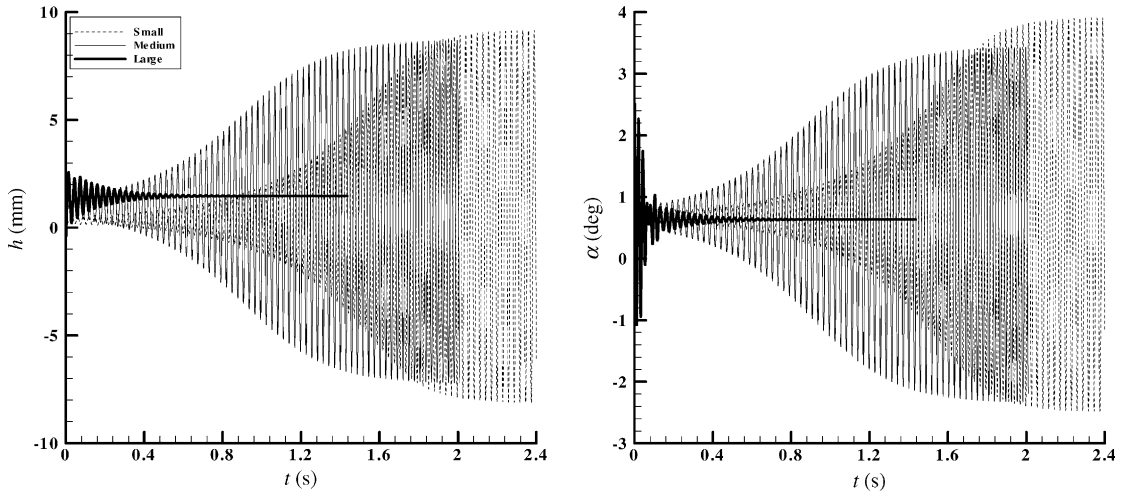

(a) Plunge mode (b) Pitch mode

Fig. 9. Effect of initial perturbation sizes: (a) plunge motion; (b) pitch motion.

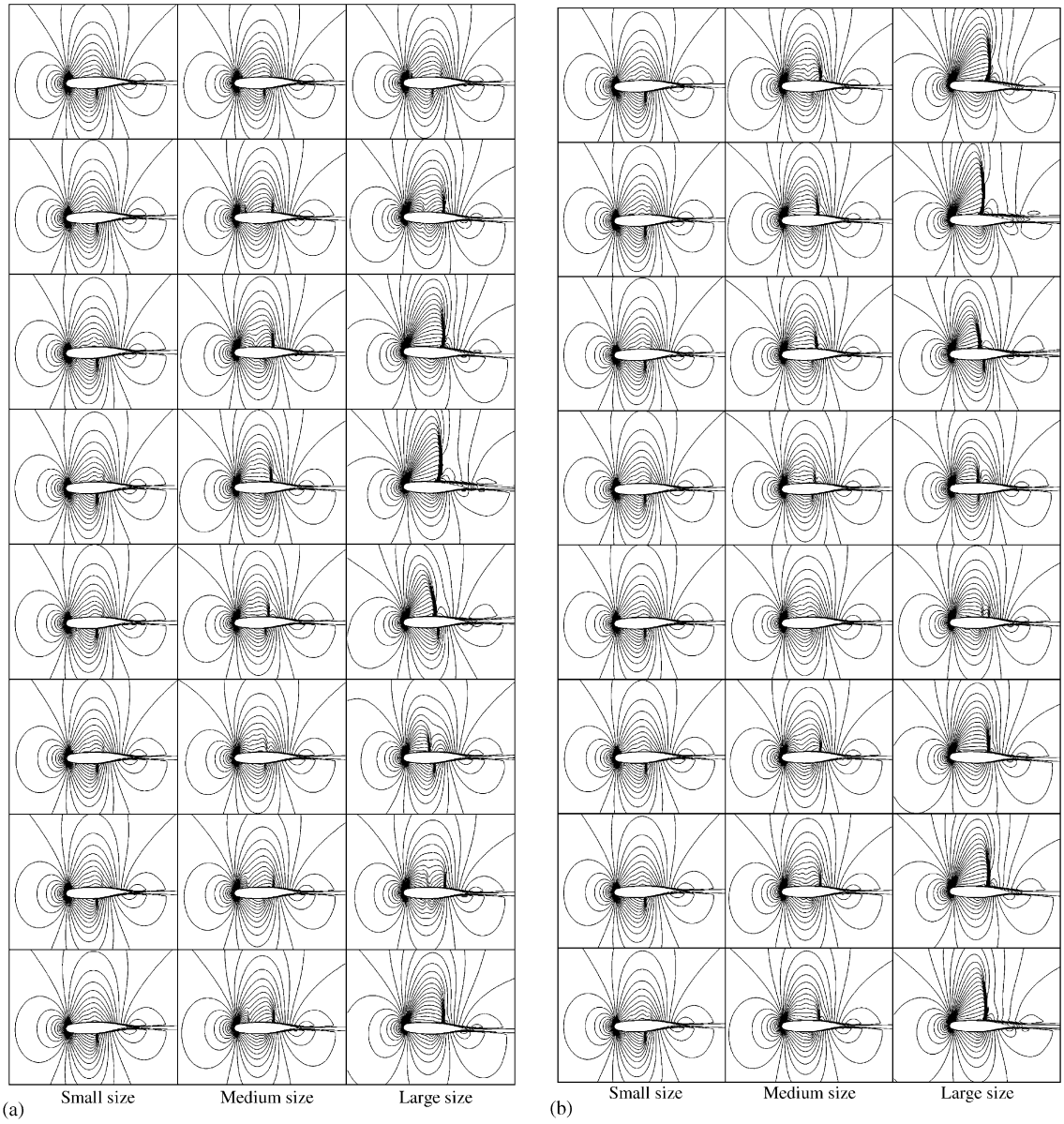

Fig. 10. Density contours showing effect of initial perturbation sizes: (a) 1st cycle; (b) 2nd cycle; (c) 3rd cycle; (d) final LCO cycle.

phenomena, Fig. 10 further compares the predicted density contours at 32 time steps uniformly distributed in the first three cycles and the last fully LCO cycle for the three different sizes of perturbation side-by-side. It is found that for the small perturbation, initially there is only mild shock and boundary layer separation present in the flowfield. The lack of strong nonlinearity in the flowfield allows the amplitudes of both plunge and pitch motions to grow gradually up to the values which cause strong shocks and large boundary layer separation, as shown in Fig. 10(d). Then an LCO forms. It is also found that for the small perturbation, initially the flowfield does not change too much from cycle to cycle. Therefore the final LCO mean airfoil position does not shift. For the medium perturbation, a similar process happens except that stronger shocks exist initially. After the first cycle, the airfoil does not go back to the original position and the flow patterns of the second cycle do not repeat those of the first cycle. Therefore the final LCO mean airfoil position shifts slightly. This can be seen by comparing Fig. 10(a) with Fig. 10(d). Finally, the flow patterns for the large perturbation are quite different from those for the small and medium perturbations. Very strong shocks and large boundary layer separation exist even in the first cycle. The resulting nonlinear effect damps the amplitudes of both

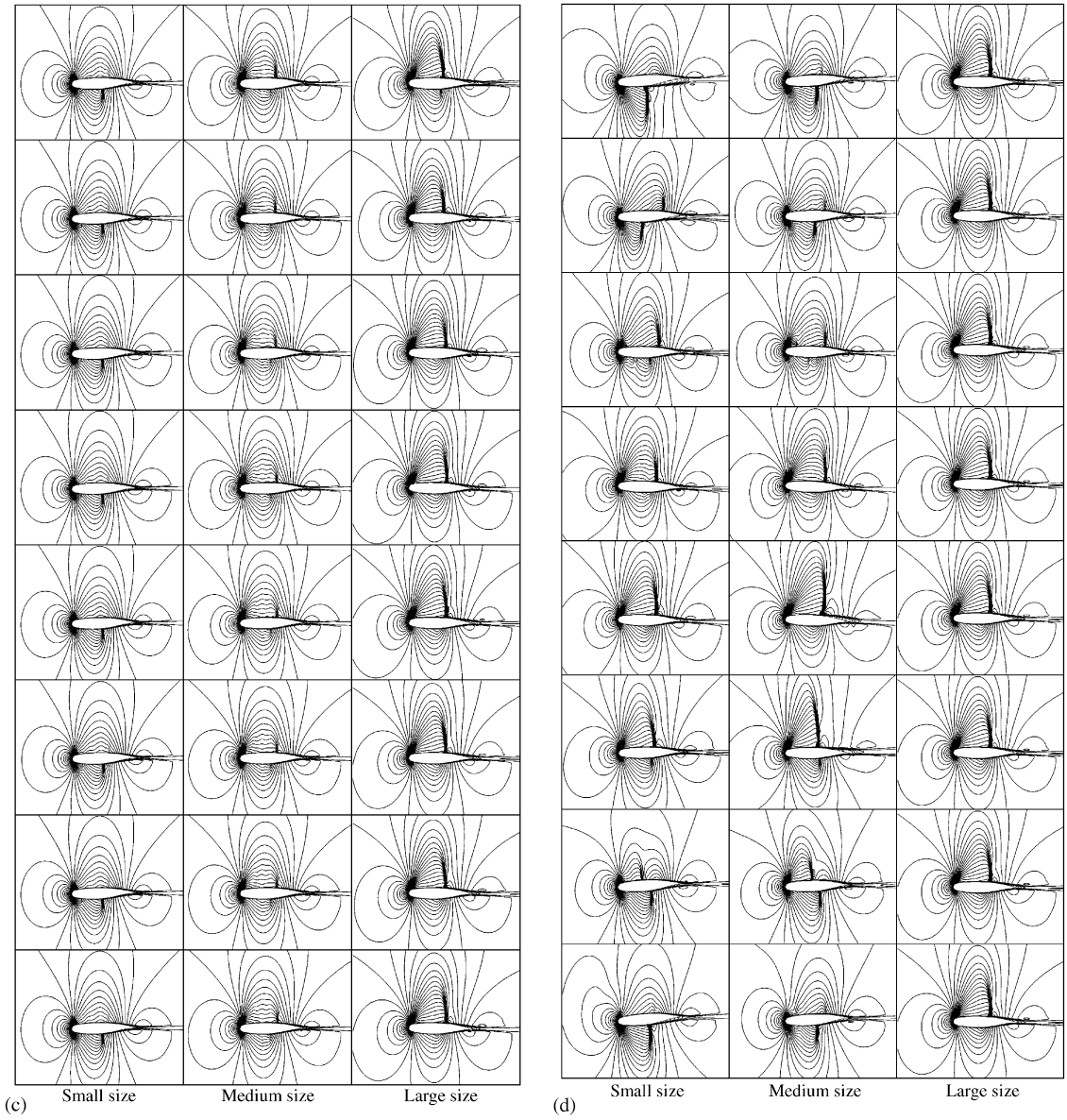

Fig. 10 (*continued*).

plunge and pitch motions from the beginning. After the first three cycles, the flow patterns just start to be stable from cycle to cycle and the final mean airfoil plunge and pitch positions shift. In the cases initiated by large amplitude perturbations that were examined, nonlinear aerodynamic effects tend to reduce and eventually eliminate LCO amplitudes. However, the range of parameters investigated is relatively limited. A more extensive study (both numerically and experimentally) on this topic is needed.

4. Conclusions

A numerical study has been conducted to investigate the impact of nonlinear aerodynamics, such as the viscosity, turbulence modelling and the initial perturbation sizes, on the transonic LCO behaviors. It has been found that the Navier–Stokes computed LCO amplitude is less than $\frac{1}{3}$ of that as determined by an Euler computation and is much

closer to the experimental data. However, it has been observed that the Navier–Stokes computation of LCO is quite dependent on the turbulence model employed. The Degani–Schiff modification to the Baldwin–Lomax turbulence model provokes spurious vorticity spots causing multiple shocks which might be unphysical, while the Spalart–Allmaras turbulence model yields physically reasonable unsteady shocks. The initial perturbation intensity has a strong influence with an unexpected diminishing effect on the amplitudes of the computed limit cycle. Also affected by the initial perturbation are the LCO mean airfoil plunge and pitch positions.

Acknowledgements

The authors gratefully acknowledge Dr. Schewe of DLR for his consultation on the LCO experimental set-up and its structural design. They also like to thank Prof. Platzer of Naval Postgraduate School, and Dr. Weber of DaimlerChrysler Aerospace for their help in providing us with CFD data. The ZONA Technology authors (Tang, Chen, and Liu) would like to acknowledge AFOSR (Dr. Sanders and Dr. Segalman are technical monitors) for its sponsorship of the present work under STTR phase I contract.

References

Bartels, R.E., 2000. Mesh strategies for accurate computation of unsteady spoiler and aeroelastic problems. Journal of Aircraft 37, 521–525.

Biedron, R.T., 2002. http://fmad-www.larc.nasa.gov/~biedron/Cfl3dv6/cfl3dv6.html

Castro, B.M., Ekaterinaris, J.A., Platzer, M.F., 2000. Transonic flutter computations for the NLR 7301 airfoil inside a wind tunnel. AIAA Paper 2000-0984.

Chen, P.C., Sarhaddi, D., Liu, D.D., 1998. Limit cycle oscillation studies of a fighter with external stores. AIAA Paper 98-1727.

Cunningham Jr., A.M., Meijer, J.J., 1995. Semi-empirical unsteady aerodynamics for modeling aircraft limit cycle oscillations and other nonlinear aeroelastic problems. Proceedings of the International Forum on Aeroelasticity and Structural Dynamics, Royal Aeronautical Society, London.

Cunningham, H.J., Batina, J.T., Bennett, R.M., 1988. Modern wing flutter analysis by computational fluid dynamics methods. Journal of Aircraft 25, 962–968.

Degani, D., Schiff, L., 1983. Computation of supersonic viscous flows around pointed bodies at large incidence. AIAA Paper 83-0034.

Denegri, C.M., 2000. Limit cycle oscillation flight test results of a fighter with external stores. AIAA Paper 2000-1394.

Edwards, J.W., 1996. Transonic shock oscillations and wing flutter calculated with an interactive boundary layer coupling method. Euromech-Colloquium 349 Simulation of Fluid-Structure Interaction in Aeronautics, Göttingen.

Edwards, J.W., Bennett, R.W., Whitlow, Seidel Jr., D.A., 1983. Time-marching transonic flutter solutions including angle-of-attack effects. Journal of Aircraft 20, 899–906.

Edwards, J.W., Schuster, D.M., Spain, C.V., Keller, D.F., Moses, R.W., 2001. MAVRIV flutter model transonic limit cycle oscillation test. AIAA Paper 2001-1291.

Hall, K.E., Thomas, J.P., Dowell, E.H., 1999. Reduced-order modeling of unsteady small disturbance flows using a frequency-domain proper orthogonal decomposition technique. AIAA Paper 99-0655.

Hartwich, P.M., Agrawal, S., 1997. Method for perturbing multiblock patched grids in aeroelastic and design optimization applications. AIAA Paper 97-2038.

Knipfer, A., Schewe, G., 1999. Investigations of an oscillating supercritical 2D wing section in a transonic flow. AIAA Paper 99-0653.

Knipfer, A., Schewe, G., Wendt, V., 1998. Numerische und experimentelle Untersuchungen an einem schwingenden NLR 7301-Profil in transsonischer Stroemung, Teil 1: Flattern und erzwungene Schwingungen. DLR Bericht IB 232-98 J 05.

Krist, S.L., Biedron, R.T., Rumsey, C.L., 1997. CFL3D User's Manual (version 5.0). NASA Langley Research Center, Hampton, VA.

Mignolet, M.P., Liu, D.D., Chen, P.C., 1999. On the nonlinear structural damping mechanism of the wing/store limit cycle oscillation. AIAA Paper 99-1459.

Norton, W.J., 1990. Limit cycle oscillation and flight flutter testing. Proceedings of the 21st Annual Symposium, Society of Flight Test Engineers, Lancaster, CA, USA.

Roe, P.L., 1981. Approximate Riemann solvers, parameter vectors, and difference schemes. Journal of Computational Physics 43, 357–372.

Schewe, G., Deyhle, H., 1996 Experiments on transonic flutter of a two-dimensional supercritical wing with emphasis on the non-linear effects. Proceedings of the Royal Aeronautical Society Conference on Unsteady Aerodynamics, London.

Spalart, P., Allmaras, S., 1992. A one-equation turbulence model for aerodynamic flows. AIAA Paper 92-0439.

Weber, S., Jones, K.D., Ekaterinaris, J.A., Platzer, M.F., 2001. Transonic flutter computations for the NLR 7301 supercritical wing. Aerospace Science and Technology 5, 293–304.